Journal of The Electrochemical Society, **150** (3) C131-C139 (2003)
0013-4651/2003/150(3)/C131/9/$7.00 © The Electrochemical Society, Inc.

Electrodeposition of $Bi_{1-x}Sb_x$ Thin Films

P. M. Vereecken,*,[a] S. Ren, L. Sun, and P. C. Searson[z,*]

Department of Materials Science and Engineering, Johns Hopkins University, Baltimore, Maryland 21218, USA

Bismuth and antimony are semimetals with a rhombohedral crystal structure and similar lattice parameters. $Bi_{1-x}Sb_x$ alloys exhibit unusual electronic properties and are of interest for thermoelectric and magnetoelectronic devices. In this paper, we show that $Bi_{1-x}Sb_x$ alloys can be electrodeposited from acidic chloride-based solutions and that a homogenous solid solution is obtained across the entire composition range. We show that bulk deposition is preceded by monolayer deposition at potentials negative to the equilibrium potential. The deposition/stripping reaction for bismuth is more reversible than for antimony leading to a small increase in the bismuth concentration in films compared to the concentration in solution at low Sb(III) concentrations. Thin films have a preferred (012) texture and the interplanar spacing is proportional to the film composition according to Vegard's rule. The grain size for thin films increases from about 1 μm for pure Bi to several micrometers for pure Sb.
 [DOI: 10.1149/1.1545458]

Manuscript submitted March 15, 2002; revised manuscript received September 11, 2002. Available electronically January 31, 2003.

Bismuth and antimony are semimetals with unusual thermal, electrical, and magnetic transport properties. Both elements have a rhombohedral crystal structure with similar lattice parameters and form a solid solution over the entire composition range. Interest in these elements is largely due to their small carrier effective masses and hence high mobilities.[1,2] Bismuth exhibits very low carrier concentrations and long carrier mean free paths[3] leading to a very large magnetoresistance effect in bulk single crystals[4,5] or thin films grown by molecular beam epitaxy[6] or electrodeposition.[7-11] $Bi_{1-x}Sb_x$ alloys are semimetals over most of the compositional range but are semiconductors for $0.07 < x < 0.22$, with a maximum band gap of about 30 meV at about $x = 0.16$.[1]

There have been relatively few studies of electrodeposition of Bi, Sb, or BiSb thin films (*e.g.*, Ref. 12-18). Both Bi and Sb can be deposited from chloride or perchlorate solutions at sufficiently low pH so that the formation of the oxyanion can be avoided. In this paper, we report on the deposition of $Bi_{1-x}Sb_x$ alloy thin films from acidic chloride solution. We show that a homogenous solid solution can be formed across the entire composition range.

Experimental

Electrochemical measurements were performed under ambient conditions in a three-electrode cell with a platinum counter electrode and a Ag/AgCl (3M $NaCl_{(aq)}$) reference electrode [$U_{eq} = 0.215$ V (saturated hydrogen electrode, SHE)] positioned close to the working electrode using a Luggin capillary. The working electrode was a 200 nm thick polycrystalline gold film evaporated onto a Si(100) wafer with a 15 nm Cr adhesion layer. The electrode area was 0.2 cm^2. Electrical contact to the gold films was made with colloidal silver paste (Electron Microscopy Sciences). The solution used for deposition of $Bi_{1-x}Sb_x$ alloys was an aqueous solution of $(0.1 - y)$ M $BiCl_3$ + y M $SbCl_3$ + 2.4 M HCl + 0.03 M ethylenediaminetatracetic acid (EATA) with the $SbCl_3$ concentration, y, ranging between 0 and 0.1 M. Prior to each experiment the Au surface was etched with 10 vol % HNO_3 for 30 s, rinsed with distilled, deionized (DI) water, rinsed with 2.4 M HCl, and finally rinsed with the $(0.1 - y)$ M $BiCl_3$ + y M $SbCl_3$ solution.

The deposition efficiency was determined by depositing films at constant potential for 50 s and then stripping by scanning the potential to +0.4 V at a scan rate of 10 mV s^{-1}. The deposition efficiency was determined from the ratio of the stripping charge to the deposition charge for solutions with 0% Sb, 18% Sb, 70% Sb, and 100% Sb.

$Bi_{1-x}Sb_x$ films for physical characterization were electrodeposited at 7 mA cm^{-2} for 200 s using a two-electrode arrangement. The substrate was a 100 nm thick gold film sputter deposited on a Si(100) wafer with a presputtered Cr adhesion layer. The deposition charge of 1.4 C cm^{-2} corresponds to a film thickness of 1.0 μm for Bi and 0.88 μm for Sb, assuming 100% deposition efficiency. The area of the film was 1.43 cm^2. After deposition, the films were thoroughly rinsed with 1 M HCl, rinsed with distilled, DI water, and finally dried in a nitrogen flow.

X-ray diffraction (XRD) measurements were performed on a Philips X'pert X-ray diffractometer using a Cu Kα source. All scans were performed with a step width of 0.01° and at a scan rate of 0.02° s^{-1}. The instrument was calibrated before each measurement using the Si(004) peak. The composition of the deposited films was determined from wavelength dispersive X-ray spectroscopy (WDS) using a Jeol 8600 Superprobe. Compositions were obtained using a 20 μm diam beam taking the average of ten measurements at different locations on the film.

Speciation

Figure 1 shows the concentration of the relevant Bi(III) and Sb(III) chloride complexes *vs.* the mole fraction of Sb in solution for a total metal ion concentration [Bi(III) + Sb(III)] of 0.1 M. The solution composition was calculated from the stability constants β_n for $BiCl_n^{3-n}$,[19] and $SbCl_n^{3-n}$,[20] summarized in Table I. The details are provided in the Appendix. The concentration of uncomplexed Bi^{3+} and Sb^{3+} ions is negligibly small; for a 0.1 M $BiCl_3$ solution, the Bi^{3+} concentration is 1.60×10^{-10} M; for a 0.1 M $SbCl_3$ solution, the Sb^{3+} concentration is 3.0×10^{-8} M. Figure 1b shows the percentage of each Bi(III) and Sb(III) complex with respect to the total Bi(III) or Sb(III) concentration *vs.* the mole fraction of Sb in solution. This figure illustrates that the hexachloride and pentachloride complexes are the dominant bismuth species in solution at about 60 and 40%, respectively. The pentachloride, hexachloride, and tetrachloride complexes are the main antimony species at 50, 25, and 20%, respectively. In all cases, the percentages are almost independent of the Sb/Bi ratio in solution.

For the case of antimony, even at low pH, the concentration of the antimonyl cation SbO^+ must also be considered[21]

$$SbO^+(aq) + 2H^+(aq) + 3e- \leftrightarrow Sb(s) + H_2O \qquad [1]$$

The formation of the oxyion from uncomplexed Sb^{3+} ions and water is given by

$$Sb^{3+}(aq) + H_2O \leftrightarrow SbO^+(aq) + 2H^+(aq) \qquad [2]$$

[a] Present address: IBM T. J. Watson Research Center, Yorktown Heights, New York 10598.
* Electrochemical Society Active Member.
[z] E-mail: searson@jhu.edu

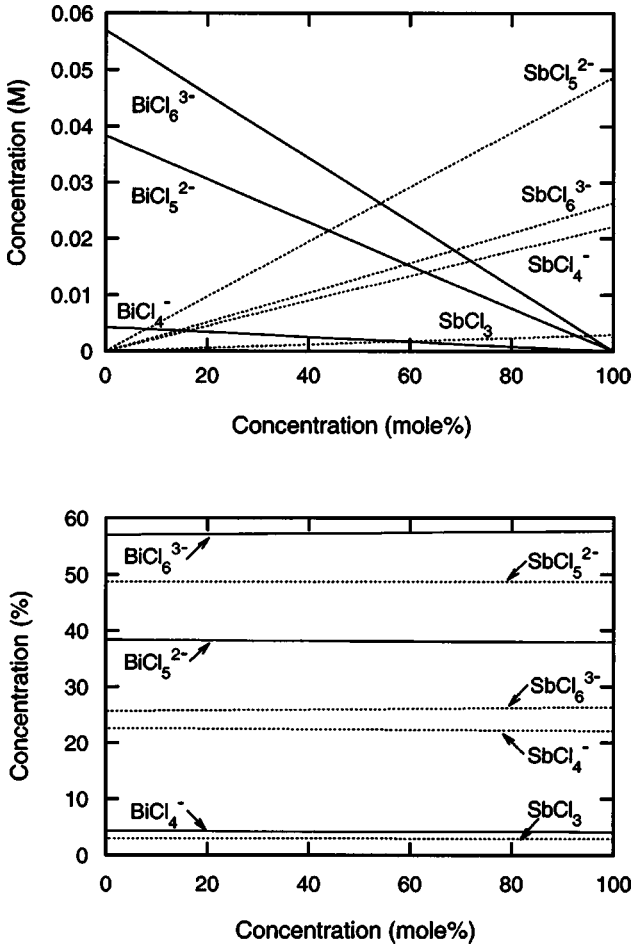

Figure 1. (a) Concentration of relevant Bi(III) and Sb(III) chloride complexes in solution *vs.* the mole percent of Sb(III) in solution, for a total metal ion concentration [Bi(III) + Sb(III)] of 0.1 M. (b) Percentage of Bi(III) and Sb(III) chloride complexes with respect to the total Bi(III) or Sb(III) concentration *vs.* the mole percent of Sb(III) in solution. Note that the concentrations of Sb^{3+}, Bi^{3+}, and SbO^{+} are negligible.

The equilibrium constant, K_{eq}, for Reaction 2 can be determined from the standard potential for the Sb^{3+}/Sb redox couple [$U^{o}_{Sb^{3+}/Sb} = 0.26$ V (SHE)] and the Nernst equation for Reaction 1 with $U^{o}_{SbO^{+}/Sb} = 0.204$ V (SHE)

$$K_{eq} = \frac{[SbO^{+}][H^{+}]^2}{[Sb^{3+}]} = 9.8 \times 10^2 \text{ mol}^2\text{L}^{-2} \quad [3]$$

For an H^{+} concentration of 2.4 M, the SbO^{+} concentration is 1.8×10^{-6} M for a 0.1 M $SbCl_3$ solution. This concentration is negligibly small and can be neglected.

The standard potentials for the bismuth chloride and antimony chloride complexes, denoted as $U^{o}_{MCl_n^{3-n}/M}$ with M = Bi or Sb, are related to the standard potentials of the uncomplexed Bi^{3+} and Sb^{3+} ions, $U^{o}_{M^{3+}/M}$, through their respective stability constants β_n and at 298 K

$$U^{o}_{MCl_n^{3-n}/M} = U^{o}_{M^{3+}/M} - \frac{RT}{3F}\log\beta_n = U^{o}_{M^{3+}/M} - 0.0197\log\beta_n \quad [4]$$

Reliable values of the standard potentials for the Bi^{3+}/Bi and Sb^{3+}/Sb couples are not known, since complexation and hydrolysis generally results in very small concentrations of uncomplexed Bi^{3+} and Sb^{3+} ions.[19,22,23] As a result, the Bi^{3+}/Bi and Sb^{3+}/Sb redox potentials are obtained indirectly through measurements of their compounds and subsequent thermodynamic calculations.

For the Bi^{3+}/Bi equilibrium

$$Bi^{+}(aq) + 3e^{-} \leftrightarrow Bi(s) \quad [5]$$

values of the standard potential reported in the literature are in the range 0.20 to 0.32 V (SHE).[19,21,22,24]

For the $BiCl_4^{-}/Bi$ equilibrium

$$BiCl_4^{-}(aq) + 3e^{-} \leftrightarrow Bi(s) + 4Cl^{-}(aq) \quad [6]$$

the standard potential $U^{o}_{BiCl_4^{-}/Bi}$, calculated indirectly from the oxychloride compound, is 0.16 V (SHE).[19,22,24] The standard potential for the Bi^{3+}/Bi couple calculated from the standard potential of the tetrachloro complex and its stability constant β_4 (see Table I) using Eq. 4 is $U^{o}_{(Bi^{3+}/Bi)} = 0.28$ V (SHE).

For the Sb^{3+}/Sb equilibrium

$$Sb^{3+}(aq) + 3e^{-} \leftrightarrow Sb(s) \quad [7]$$

values for the standard potential are not available in the literature. For the antimony tetrachloride complex

$$SbCl_4^{-}(aq) + 3e^{-} \leftrightarrow Sb(s) + 4Cl^{-}(aq) \quad [8]$$

the standard potential $U^{o}_{SbCl_4^{-}/Sb} = 0.17$ V (SHE).[19,23] From the value for $U^{o}_{SbCl_4^{-}/Sb}$ and the stability constant β_4 (see Table I), the standard potential for uncomplexed Sb^{3+} ions determined from Eq. 4 is $U^{o}_{Sb^{3+}/Sb} = 0.26$ V (SHE).

The equilibrium potentials for bismuth and antimony for any solution composition can be determined either from the concentration of uncomplexed M^{3+} ions or from the concentration of the chloride complexes MCl_n^{3-n} in solution using the Nernst equation. For the uncomplexed M^{3+} ions we obtain

$$U_{eq} = U^{o}_{M^{3+}/M} + 0.0197\log[M^{3+}] \quad [9]$$

For the chloride complexes MCl_n^{3-n} we obtain

$$U_{eq} = U^{o}_{(MC_n^{3-n}/M)} + 0.0197\log\frac{[MCl_n^{3-n}]}{[Cl^{-}]^n} \quad [10]$$

The standard potentials for the different $BiCl_n^{3-n}$ and $SbCl_n^{3-n}$ species calculated from Eq. 4 are summarized in Table II. The stan-

Table I. Stability constants $\beta_n = [MCl_n^{n-3}]/[M^{3+}][Cl^{-}]^n$.

M	β_1	β_2	β_3	β_4	β_5	β_6
Bi	2.3×10^2	3.1×10^3	2.24×10^5	1.26×10^6	5.25×10^6	3.63×10^6
Sb	1.8×10^2	3.1×10^3	1.5×10^4	5.3×10^4	5.2×10^4	1.3×10^4

Table II. Standard potentials $U^{o}_{(MCl_n^{3-n}/M)}$ (V *vs.* SHE) for uncomplexed metal ions ($n = 0$) and metal chloride complexes (for $1 \leq n \leq 6$) determined from Eq. 4 and the stability constants given in Table I. $MCl_n^{3-n} + 3e^- \leftrightarrow M + nCl^-$.

	$n = 0$	$n = 1$	$n = 2$	$n = 3$	$n = 4$	$n = 5$	$n = 6$
$U^{o}_{(BiCl_n^{3-n}/Bi)}$	0.28	0.23	0.21	0.17	0.16	0.15	0.15
$U^{o}_{(SbCl_n^{3-n}/Sb)}$	0.26	0.22	0.19	0.19	0.17	0.17	0.18

dard potentials for the chloride complexes of both elements with $n > 2$ are very close indicating that bismuth and antimony will codeposit as an alloy even at low overpotentials.

In summary, well defined values for $U^{o}_{M^{3+}/M}$ and $U^{o}_{MCl_n^{3-n}/M}$ are not available. In the literature, the standard potentials for the tetrachloro complexes are $U^{o}_{BiCl_4^-/Bi} = 0.16$ V (SHE) (determined indirectly) and $U^{o}_{SbCl_4^-/Sb} = 0.17$ V (SHE). The standard potentials for the Bi^{3+}/Bi and Sb^{3+}/Sb couples obtained from the tetrachloro complexes using the relevant stability constants are $U^{o}_{Bi^{3+}/Bi} = 0.28$ V (SHE) and $U^{o}_{Sb^{3+}/Sb} = 0.26$ V (SHE).

Results and Discussion

Figure 2 shows current-potential curves for gold in $(0.1 - y)$ M $BiCl_3$ + y M $SbCl_3$ + 2.4 M HCl + 0.03 M EDTA, with Sb(III) mole fractions from 0% ($y = 0$) to 100% ($y = 0.1$ M). All solutions exhibit characteristic bulk deposition and stripping peaks. The separation between the peaks increases with increasing Sb(III) concentration in solution indicating that deposition and stripping become more irreversible with increasing Sb(III) concentration. The decrease in the peak current density with increasing Sb(III) concentration is also indicative of increasing irreversibility.[25] Underpotential deposition was observed between the open-circuit potential (OCP) (+0.5 V *vs.* Ag/AgCl) and −0.1 V for all solutions, but is not considered further here.

The equilibrium potentials for the Bi(III)/Bi and Sb(III)/Sb couples can be experimentally identified from the potential of zero current in the reverse scan. The standard potentials can subsequently be determined using Eq. 9 and 10. Figure 3 shows the potential of

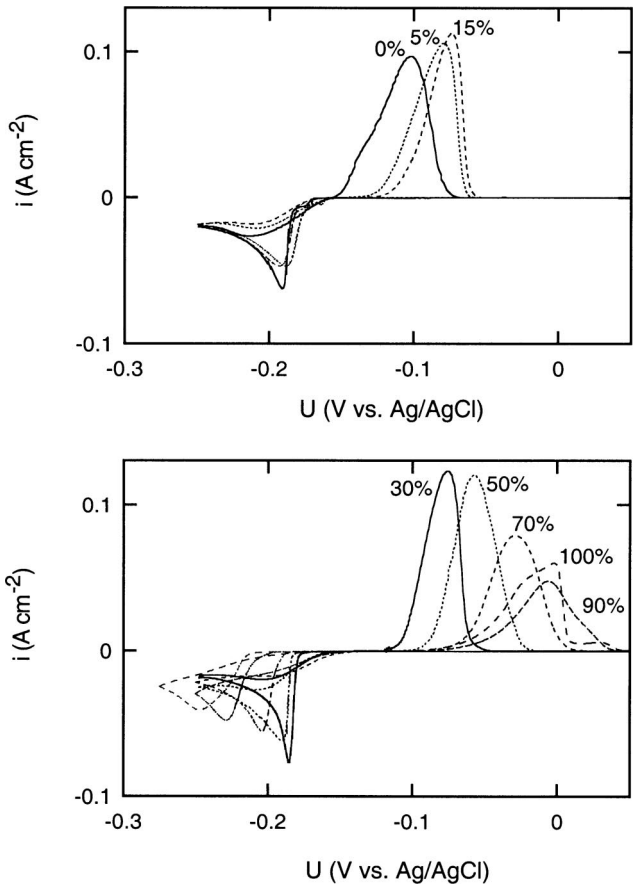

Figure 2. Current/voltage curves for $(0.1 - y)$ M $BiCl_3$ + y M $SbCl_3$ + 2.4 M HCl + 0.03 M EDTA, with Sb(III) mole fractions from 0% ($y = 0$) to 100% ($y = 0.1$ M). The mole percent of Sb(III) in the solution is indicated in the figure. The scan rate was 10 mV s^{-1}.

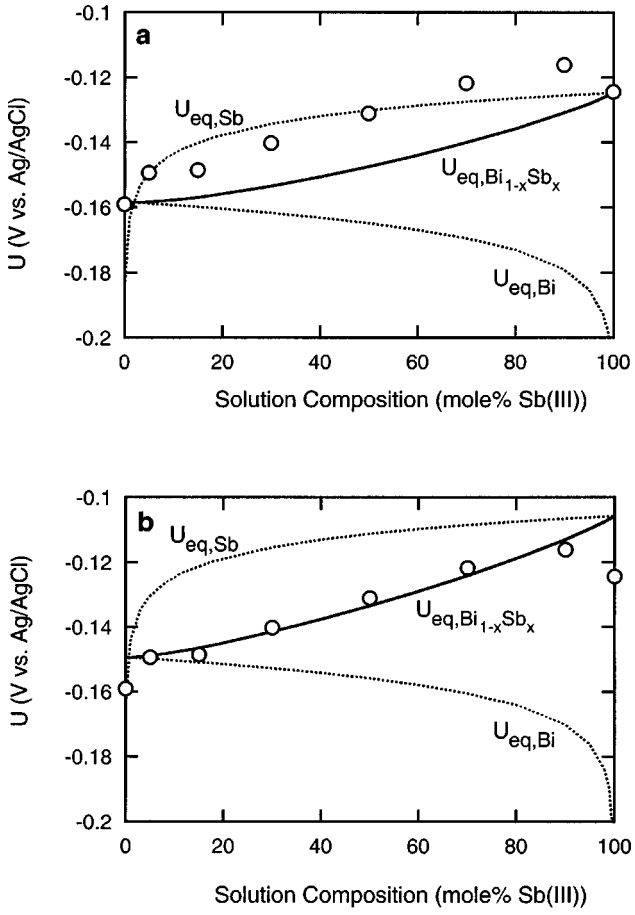

Figure 3. (○) Zero-current potential, $U_{i=0}$, obtained from the reverse scan in current/voltage curves for solutions with $(0.1 - y)$ M $BiCl_3$ + y M $SbCl_3$ with y varying from 0 to 0.1 M. The dashed lines show the equilibrium potentials for the Bi(III)/Bi and Sb(III)/Sb couples *vs.* the mole percent of Sb(III) in solution calculated (a) from the experimental equilibrium potentials for the pure components ($U_{eq,Bi} = -0.16$ V; $U_{eq,Sb} = -0.12$ V) and (b) from the partial standard equilibrium potentials $U^{o}_{Bi} = U^{o}_{Sb} = U^{o}_{Bi_{1-x}Sb_x} = 0.045$ V (Ag/AgCl) determined from a best fit of $U_{i=0}$ for the mixed solutions to U_{mix}. The solid line corresponds to the mixed potential, U_{mix}, for the two component mixed solution calculated assuming a rule of mixtures for the pure components in a and b.

zero current in the reverse scan, $U_{i=0}$, obtained from solutions with $(0.1 - y)$ M $BiCl_3$ + y M $SbCl_3$.

In 0.1 M $BiCl_3$ solution, $U_{i=0,Bi} = -0.16$ V *vs.* Ag/AgCl ($U_{eq,Bi} = 0.055$ V *vs.* SHE). For the 0.1 M $SbCl_3$ solution, $U_{i=0,Sb} = -0.12$ V *vs.* Ag/AgCl ($U_{eq,Sb} = 0.095$ V *vs.* SHE). From Eq. 9 it follows that $U^{o}_{Bi^{3+}/Bi} = 0.25$ V (SHE) and $U^{o}_{Sb^{3+}/Sb} = 0.24$ V (SHE), close to the literature values obtained from the tetrachloride complexes.

The equilibrium potentials for the Bi(III)/Bi and Sb(III)/Sb couples in mixed solutions ($U_{eq,Bi}$ and $U_{eq,Sb}$,) can now be calculated for all solution compositions from the values of $U^{o}_{M^{3+}/M}$ using Eq. 9 and the speciation data. The dependencies of $U_{eq,Bi}$ and $U_{eq,Sb}$ on Sb(III) concentration in solution, calculated from the standard potentials for pure Bi and Sb solutions, are shown in Fig. 3a. For a simple rule of mixtures, the equilibrium potential for the two component system is given by

$$U_{mix} = (1 -)U_{eq,Bi} + xU_{eq,Sb} \quad [11]$$

where $0 < x < 1$. The variation of U_{mix} with solution composition is also shown Fig. 3a. It can be seen that there is about a 20 mV difference between the experimentally measured potentials for the mixed solutions ($U_{i=0,BiSb}$) and U_{mix} calculated from the zero current potentials for the pure solutions. However, fitting the experimental $U_{i=0}$ values for the mixed solutions to U_{mix} by adjusting the equilibrium potentials for Bi and Sb ($U_{eq,Bi}$ and $U_{eq,Sb}$) resulted in a good correlation between $U_{i=0}$ and U_{mix}, as demonstrated in Fig. 3b. The fit shown in Fig. 3b was obtained for

$$U^{o}_{Bi} = U^{o}_{Sb} = U^{o}_{Bi_{1-x}Sb_x} = 0.26\ \text{V(SHE)} \quad [12]$$

where $U^{o}_{Bi_xSb_{1-x}}$ is the standard potential for the alloy. The origin of the approximately 20 mV difference between the equilibrium potentials for the mixed solutions and the equilibrium potentials for the pure solutions is not known. Substitution of the equilibrium potentials into Eq. 11 using the Nernst equation then yields an expression for the equilibrium potential of the Bi_xSb_{1-x} alloy. At 298 K

$$U_{Bi_{1-x}Sb_x} = U^{o}_{Bi_{1-x}Sb_x} + \frac{0.0592}{3}\log([Bi^{3+}]^{1-x}[Sb^{3+}]^{x}) \quad [13]$$

Equation 13 represents the Nernst equation for the electrochemical formation of a Bi_xSb_{1-x} alloy from uncomplexed Bi^{3+} and Sb^{3+} ions

$$(1 - x)Bi^{3+} + xSb^{3+} \leftrightarrow Bi_{1-x}Sb_x \quad [14]$$

The bulk deposition peak seen in the current-potential curves (Fig. 2) was in all cases preceded by one or two smaller reduction peaks, as shown in Fig. 4. Figure 4a shows the reduction peak P_a preceding the main deposition peak in 0.1 M $SbCl_3$ solution and Fig. 4b shows the reduction peak P_b preceding the main deposition peak in 0.1 M $BiCl_3$ solution. The potential dependences of the deposition (P_{bulk}, P_a, and P_b) peaks and stripping (P_{strip}) peaks on mole fraction of Sb(III) in solution are shown in Fig. 5. The potentials of the prepeaks P_a and P_b were essentially independent of Sb(III) concentration.

The peak current density associated with P_a was about -0.5 mA cm^{-2}, or about two orders of magnitude smaller than the current density of the bulk deposition peak. This peak was present at all solution compositions except at low Sb(III) concentration and is hence attributed to Sb(III) reduction. Prepeak P_b immediately preceded the bulk deposition peak but was only observed for solutions with high Bi(III) concentration [>70% Bi(III)] and is attributed to the reduction of Bi(III). The peak current density is this case was about -5 mA cm^{-2}, about one order of magnitude larger than P_a, and one order of magnitude smaller than the bulk deposition peak.

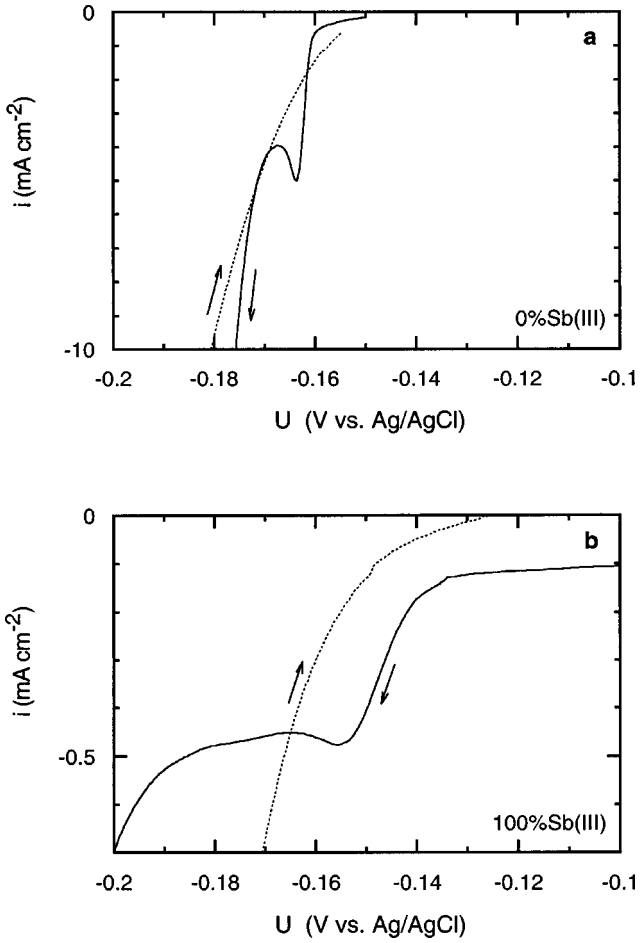

Figure 4. I-V curves for (a) 0.1 M $SbCl_3$ solution showing prepeak P_a and (b) 0.1 M $BiCl_3$ solution showing prepeak P_b. The scan rate was 10 mV s^{-1}.

When the scan direction was reversed at a potential slightly positive to the onset of the bulk deposition peak, a distinct stripping peak was observed in the reverse scan, indicating that prepeaks P_a and P_b are associated with deposition. The area under the prepeaks was in the range 0.5-1 mC cm^{-2}, close to the values for a close-packed (001) monolayer of Bi (0.54 mC cm^{-2}) and Sb (0.60 mC cm^{-2}).

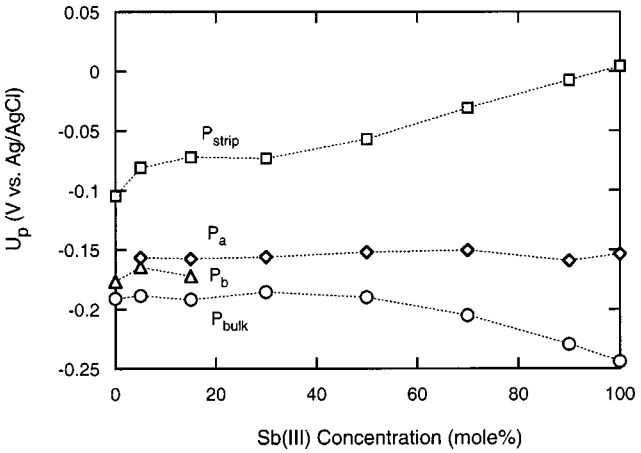

Figure 5. The potentials for the bulk deposition peak (P_{bulk}), prepeaks (P_a and P_b), and stripping peaks (P_{strip}) *vs.* mole percent of Sb(III) in solution. All data obtained from I-V curves at a scan rate of 10 mV s^{-1}.

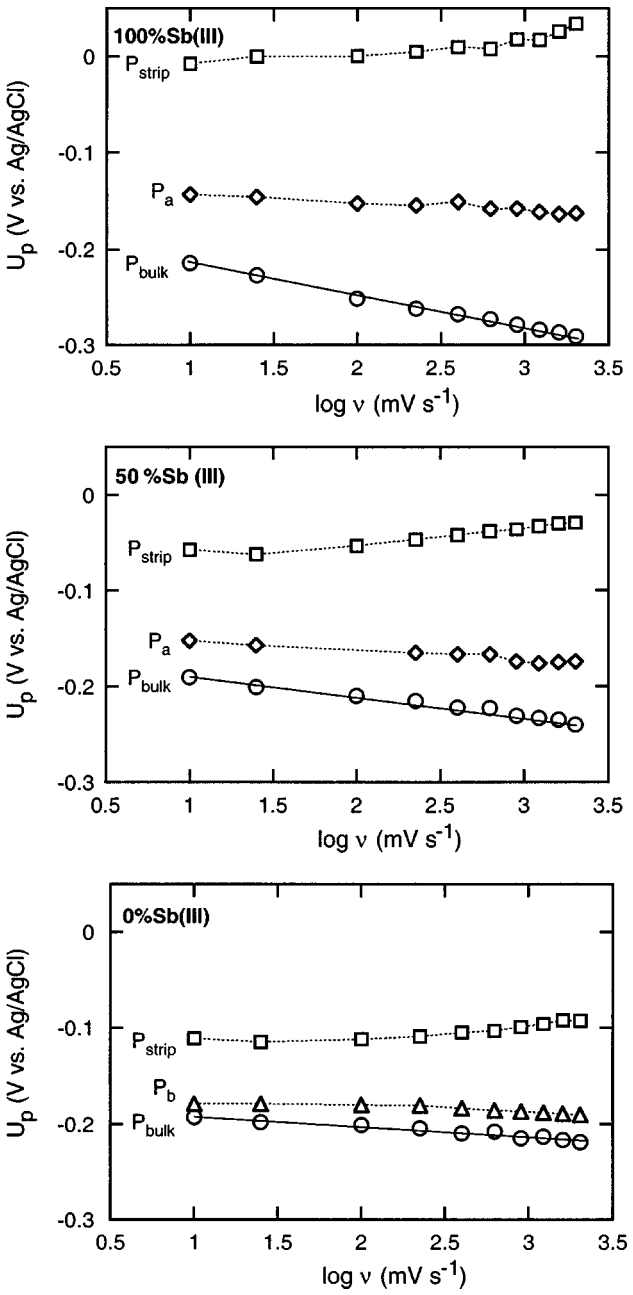

Figure 6. Peak potentials log ν for (top) 0% Sb(III), (middle) 50% Sb(III), and (bottom) 100% Sb(III).

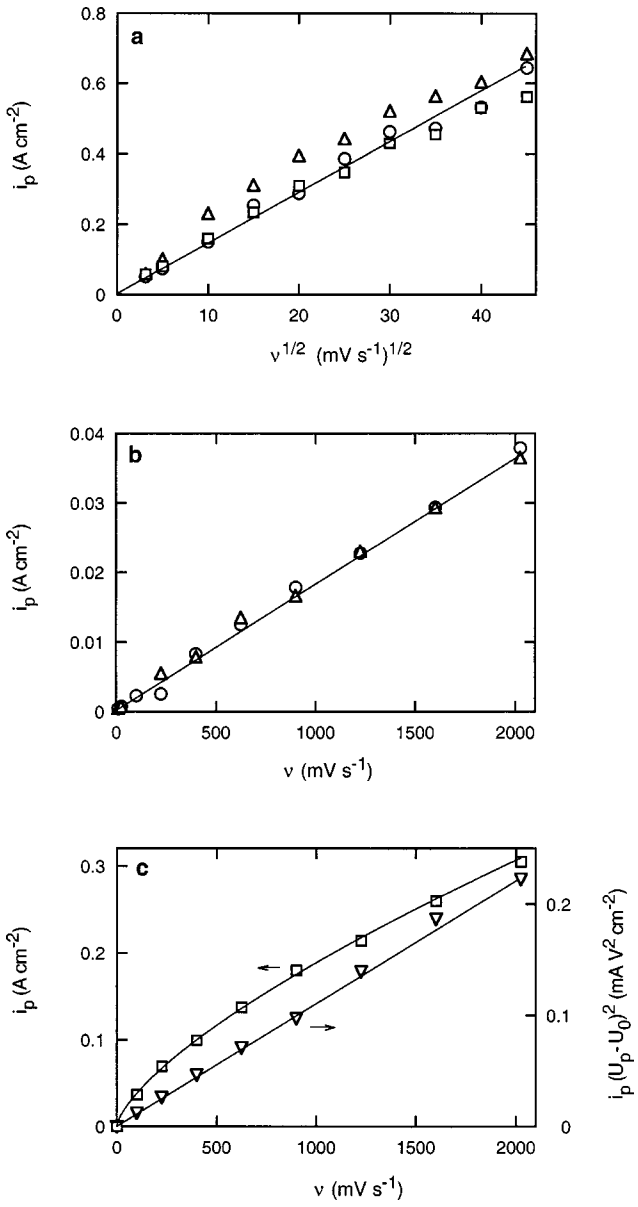

Figure 7. (a) Current density of the bulk deposition peak *vs.* $\nu^{1/2}$ for (□) 0% Sb(III), (△) 50% Sb(III), and (○) 100% Sb(III). (b) Current density of the prepeak P_a *vs.* ν for (△) 50% Sb(III) and (○) 100% Sb(III). (c) Current density of the prepeak P_b *vs.* ν for (□) 0% Sb(III); the solid line corresponds to $\nu^{0.7}$. Also shown is a plot of $i_p(U_p - U^o_{ea})^2$ *vs.* ν for prepeak P_b.

The separation between the bulk deposition peak and the stripping peak is about 90 mV for the 0.1 M $BiCl_3$ solution [0% Sb(III)] and 250 mV for the 0.1 M $SbCl_3$ solution [100% Sb(III)]. This illustrates the higher reversibility of the bismuth deposition/stripping reaction and the lower reversibility of the antimony deposition/stripping reaction. The bulk deposition and stripping peaks are almost independent of potential for Sb(III) concentrations $\leqslant$30%, showing that the higher reversibility of the bismuth deposition/stripping reaction is maintained up to about 30% Sb(III). For solution compositions >30% Sb(III), the peak separation between the main reduction peak and the stripping peak becomes larger with increasing Sb(III) concentration due to the lower reversibility of the deposition/stripping reaction.

Figure 6 shows the scan rate dependence of the potentials associated with the bulk deposition peak, the prepeaks, and the striping peak for 0.1 M $BiCl_3$ [0% Sb(III)], 0.05 M $BiCl_3$ + 0.05 M $SbCl_3$ [50% Sb(III)], and 0.1 M $SbCl_3$ [100% Sb(III)]. The increasing reversibility of the metal ion couples with decreasing Sb(III) concentration are again clearly seen. Accordingly, the scan rate dependence of the bulk deposition peak decreased from 30 mV/decade for 100% Sb(III) to 20 mV/decade for 50% Sb(III) to 10 mV/decade for 0% Sb(III).

Figure 7 shows the dependence of the current density associated with the bulk deposition peak, the prepeaks, and the striping peak in solutions with 0% Sb(III), 50% Sb(III), and 100% Sb(III), on scan rate. The peak current density associated with the bulk deposition peak is proportional to the square root of the scan rate, as expected for a diffusion-limited growth process. The peak current density for prepeak P_a associated with Sb deposition was proportional to the scan rate, as shown in Fig. 7b, consistent with monolayer formation either by random adsorption or by irreversible two-dimensional (2D) nucleation and growth.[25]

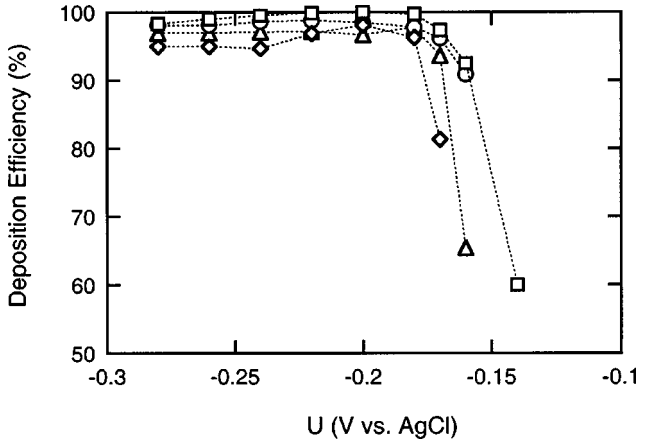

Figure 8. Deposition efficiency for films deposited at constant potential in (◇) 0% Sb(III), (○) 18% Sb(III), (△) 70% Sb(III), and (□) 100% Sb(III) solution.

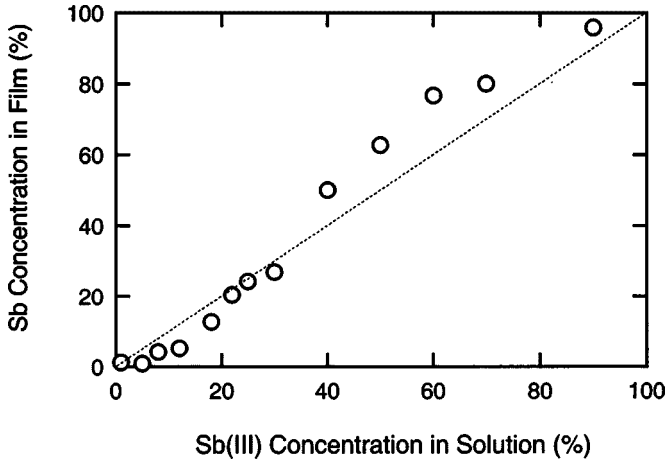

Figure 9. Concentration of Sb in films *vs.* the mole percent of Sb(III) in solution. In all cases, 1.4 C cm^{-2} films were deposited at a constant current density of 7 mA cm^{-2}. The antimony concentration in the film was determined from WDS measurements.

The scan rate dependence of the current density for prepeak P_b, associated with Bi deposition, exhibited an exponent of 0.7, *i.e.*, between $\nu^{0.5}$ and $\nu^{1.0}$, as shown in Fig. 7c. Such behavior is consistent with models for reversible monolayer formation by 2D nucleation and growth.[25] The peak current density i_p and peak potential U_p for this process are given by

$$i_p = \frac{0.368}{a} K^2 q_m \nu \quad [15]$$

$$U_p = U_a^o + \frac{a}{K} \quad [16]$$

where q_m is the charge associated with monolayer deposition, ν is the scan rate, U_a^o is the equilibrium potential for adsorption, and a is constant associated with nucleation.[b] The constant K is given by

$$K = -9.04 + 2.303 \log\left[\frac{N_0}{N_T}\left(\frac{k_n^o k_g^{o^2}}{n^6 a^3 \nu^3}\right)\right] \quad [17]$$

where N_0 is the number of active sites, N_T the total number sites per unit area, k_n^o is the standard rate constant for nucleation, and k_g^o is the standard rate constant for growth. Since K is dependent on scan rate, the peak potential and peak currents are also dependent on scan rate. Substitution of K from Eq. 16 into Eq. 15 gives

$$i_p(U_p - U_a^o)^2 = 0.368 a q_m \nu \quad [18]$$

For a reversible process, the standard adsorption potential can be approximated by the onset potential for deposition. Figure 7c shows the scan rate dependence of $i_p(U_p - U_{ea}^o)^2$ for prepeak P_b substituting the onset potential for the adsorption potential. The linear dependence of $i_p(U_p - U_{ea}^o)^2$ on scan rate is consistent with Eq. 18. The slope in Fig. 7c corresponds to $0.368 a q_m$. The parameter a can be obtained from the dependence of the peak potential on scan rate. Combining Eq. 16 and 17 we obtain

$$(U_p - U_a^a)^{-1} = -\frac{9.04}{a} + \frac{2,303}{a}\log\left[\frac{N_0 k_n^o k_g^2}{N_T n^6 a^3}\right] + \frac{6.91}{a}\log\nu \quad [19]$$

[b] $a = -\pi^2 r^2 \sigma^2 / nekT$ where r is the island radius, σ is the energy per unit area, n is the number of electrons, e is the charge on the electron, k is the Boltzmann constant, and T is temperature.[25]

A plot of $(U_p - U_{onset})^{-1}$ *vs.* $\log \nu$ for P_b was linear from which we obtained $a = 0.45$. From the slope in Fig. 7c and taking $a = 0.45$ we obtain $q_m = 0.68$ mC cm^{-2}, close to the value for a close-packed (001) monolayer of Bi (0.54 mC cm^{-2}).

From the analysis of the two prepeaks, we conclude that bulk deposition is preceded by a 2D nucleation and growth process. However, this 2D process occurs at potentials negative to the equilibrium potential and hence is not underpotential deposition. Growth of Bi on GaAs[26] and Bi on Si[27] from the vapor phase also proceeds through 2D layer formation followed by 3D island growth. An initial 2D process preceding 3D deposition at potentials negative to the equilibrium potential has been reported for electrodeposition of Ag on Ag.[28]

Figure 8 shows the deposition efficiency for films deposited at constant potential. In all cases the deposition efficiency is between 95 to 100% for potentials negative to about −0.175 V (Ag/AgCl). The point at which the efficiency becomes close to 100% corresponds to potentials between the pre-peak and the bulk deposition peak in the current-potential curves.

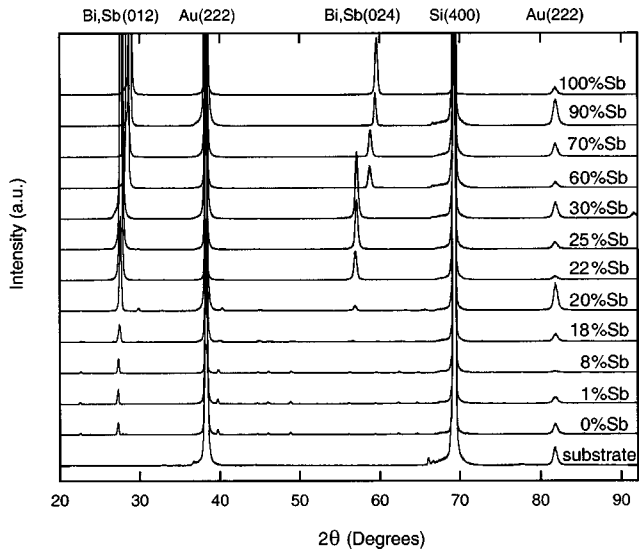

Figure 10. XRD patterns for a series of $Bi_{1-x}Sb_x$ films. The curves are displaced for clarity.

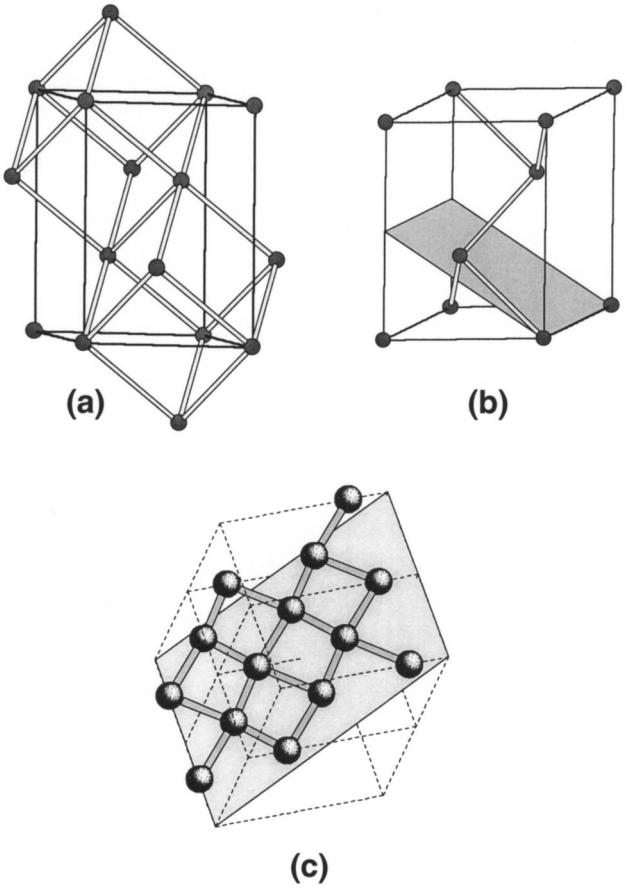

Figure 11. Crystal structure of Bi and Sb. (a) Two rhombohedral unit cells on hexagonal axes. For Bi: $a = 0.474$ nm, $\alpha = 57.233°$. (b) The hexagonal primitive cell has atoms on the corners of the parallelepiped as well as atoms at the (2/3,1/3,1/3) and (1/3,2/3,2/3) positions. For Bi: $a = b = 0.455$ nm, $c = 1.186$ nm, $\alpha = \beta = 90°$, $\gamma = 120°$; for Sb: $a = b = 0.431$ nm, $c = 1.127$ nm, $\alpha = \beta = 90°$, $\gamma = 120°$. The (012) plane is also shown. (c) Normal view to the (012) plane, illustrating the two-fold symmetry in this plane.

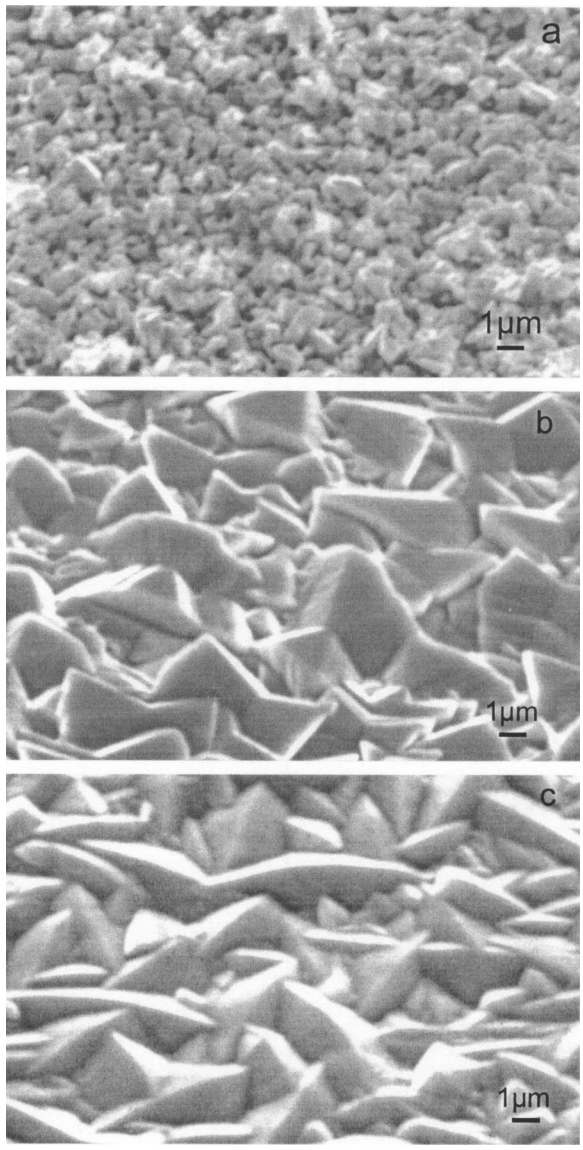

Figure 13. Scanning electron microscope plan view images for $Bi_{95}Sb_5$, $Bi_{70}Sb_{30}$, and $Bi_{10}Sb_{90}$ films.

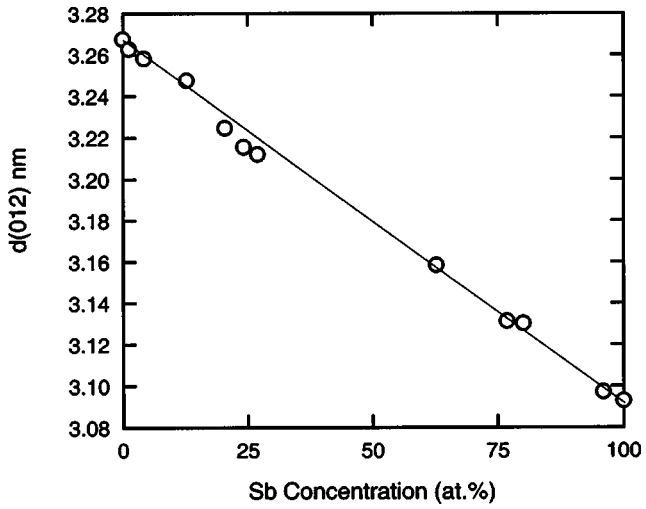

Figure 12. The lattice spacing in the (012) direction determined from the diffraction peak *vs.* the Sb concentration in the film.

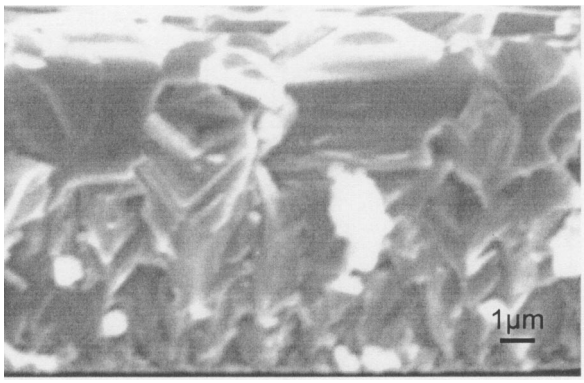

Figure 14. Cross-sectional scanning electron microscope image of a $Bi_{95}Sb_5$ film illustrating a characteristic columnar microstructure.

Thin film characterization.—Figure 9 shows the mole fraction of Sb in films deposited at 7 mA cm^{-2} *vs.* the mole fraction of Sb(III) in solution. The Sb concentration in the film is slightly lower than predicted by the linear dependence at low Sb(III) concentrations in solution (<30% Sb(III)) and slightly higher at larger Sb(III) concentrations in solution. The crossover at 30% Sb(III) corresponds to the limit of Bi-dominated reversible deposition and stripping (<30% Sb(III)). At higher concentrations of Sb(III), the deposition reaction is dominated by the more irreversible Sb deposition/stripping reaction (see Fig. 5).

Figure 10 shows XRD patterns for a series of $Bi_{1-x}Sb_x$ films. In all cases, the films are highly textured exhibiting the characteristic (012) and (024) peaks for the hexagonal crystal structure of Bi and Sb. Similar results have been reported for the electrodeposition of Bi on Au[8] and on GaAs[9,10] from acidic $Bi(NO_3)_3$ solution.

Bismuth and antimony have a rhombohedral crystal structure. For convenience, however, the crystal structures are usually represented on hexagonal axes, with a trigonal *c* axis along the [001] direction and the twofold or binary *a* and *b* axes normal to the trigonal direction and 120° apart from each other.[1] Figure 11a shows two rhombohedral unit cells on the hexagonal axes. The hexagonal primitive cell (Bi: $a = b = 0.4546$ nm, $c = 1.186$ nm, $\alpha = \beta = 90°$, $\gamma = 120°$; Sb: $a = b = 0.4308$ nm, $c = 1.127$ nm, $\alpha = \beta = 90°$, $\gamma = 120°$) shown in Fig. 11b has atoms on the corners of the parallelepiped as well as atoms at the (2/3,1/3,1/3) and (1/3,2/3,2/3) positions. The 2D unit cells for the hexagonal close-packed (001) planes of Bi and Sb are diamond shaped with sides of 0.4546 and 0.4308 nm, respectively.[1] The close-packed (001) planes are arranged in bilayers along the [001] direction[1] so that crystals are easily cleaved perpendicular to the trigonal axis. As described previously, the deposition of a close-packed (001) monolayer corresponds to 0.54 mC cm^{-2} for Bi and 0.60 mC cm^{-2} for Sb. The (012) plane is also shown in Fig. 11b. Figure 11c shows a normal view to the (012) plane, illustrating the two-fold symmetry in this plane, with two layers of atoms one slightly above and one slightly below the plane. The deposition of an (012) monolayer corresponds to 0.45 mC cm^{-2} for Bi and 0.50 mC cm^{-2} for Sb.

Figure 12 shows the lattice spacing in the (012) direction determined from the diffraction peak. This figure illustrates that the lattice spacing increases monotonically from Sb to Bi according to Vegard's rule, consistent with the formation of a homogeneous solid solution. Similar results have been reported for $Bi_{1-x}Sb_x$ films deposited at constant current.[18]

For all compositions the films were matte gray and exhibited faceted grains ranging from about 1 μm in size for pure Bi to several micrometers for pure Sb films. Figure 13 shows scanning electron microscope plan view images for $Bi_{95}Sb_5$, $Bi_{70}Sb_{30}$, and $Bi_{10}Sb_{90}$ films. These images illustrate the progressive increase in grain size with increasing Sb content. These results are consistent with the faster kinetics for bismuth deposition reaction which would be expected to lead to higher cluster density and hence smaller grain size. Figure 14 shows a cross-sectional image of a $Bi_{95}Sb_5$ film illustrating a characteristic columnar microstructure.

Conclusions

Homogeneous $Bi_{1-x}Sb_x$ alloys can be electrodeposited from acidic chloride-based solutions. Bulk deposition is preceded by monolayer deposition at potentials negative to the equilibrium potential. The deposition/stripping reaction for bismuth is more reversible than for antimony leading to a small increase in the bismuth concentration in films compared to the concentration in solution at low Sb(III) concentrations. Thin films have a preferred (012) texture and the interplanar spacing is proportional to the film composition according to Vegard's rule. The grain size for thin films increases from about 1μm for pure Bi to several micrometers for pure Sb.

Acknowledgments

This work was supported by the JHU MRSEC (NSF grant number DMR00-80031).

Johns Hopkins University assisted in meeting the publication costs of this article.

Appendix

For the determination of speciation, the following species were considered: Bi^{3+}, $BiCl_4^-$, $BiCl_5^{2-}$, $BiCl_6^{3-}$, Sb^{3+}, $SbCl_3$, $SbCl_4^-$, $SbCl_5^{2-}$, $SbCl_6^{3-}$, and Cl^-. The species $BiCl_2^+$, $BiCl_2^+$, $BiCl_3$, $SbCl_2^+$, and $SbCl_2^+$ were not considered since their stability constants are neglible.

The stability constants for bismuth and antimony are given by

$$\beta_n = \frac{[BiCl_n^{n-3}]}{[Bi^{3+}][Cl^-]^n} \quad [A1]$$

$$\beta_n^* = \frac{[SbCl_n^{n-3}]}{[Sb^{3+}][Cl^-]^n} \quad [A2]$$

The values for the relevant stability constants are given in Table I. In addition to the equilibria for the bismuth and antimony species we have five mass balance equations

$$3c_{BiCl_3} + c_{HCl} + 3c_{SbCl_3} = [Cl^-] + 4[BiCl_4^-] + 5[BiCl_5^{2-}] + 6[BiCl_6^{3-}] + 3[SbCl_3] + 4[SbCl_4^-] + 5[SbCl_5^{2-}] + 6[SbCl_6^{3-}] \quad [A3]$$

$$c_{BiCl_3} = [BiCl_4^-] + [BiCl_5^{2-}] + [BiCl_6^{3-}] = [Bi^{3+}](\beta_4[Cl^-]^4 + \beta_5[Cl^-]^5 + \beta_6[Cl^-]^6) \quad [A4]$$

$$c_{SbCl_3} = [SbCl_3] + [SbCl_4^-] + [SbCl_5^{2-}] + [SbCl_6^{3-}] = [Sb^{3+}](\beta_3^*[Cl^-]^3 + \beta_4^*[Cl^-]^4 + \beta_5^*[Cl^-]^5 + \beta_6^*[Cl^-]^5) \quad [A5]$$

$$c_{BiCl_3} + c_{SbCl_3} = 0.1\ M \quad [A6]$$

$$c_{HCl} = 2.4\ M \quad [A7]$$

Substitution of A-4, A-5, A-6, and A-7 into A-3 gives the relationship between the chloride ion concentration in solution, $[Cl^-]$, and the total concentration of bismuth chloride, c_{BiCl_3} and antimony chloride c_{SbCl_3} added to the solution

$$([Cl^-] - 2.7) + (0.1 - c_{SbCl_3})\left\{\frac{4\beta_4[Cl^-]^4 + 5\beta_5[Cl^-]^5 + 6\beta_6[Cl^-]^6}{\beta_4[Cl^-]^4 + \beta_5[Cl^-]^5 + \beta_6[Cl^-]^6}\right\} + c_{SbCl_3}\left\{\frac{3\beta_3^*[Cl^-]^3 + 4\beta_4^*[Cl^-]^4 + 5\beta_5^*[Cl^-]^5 + 6\beta_6^*[Cl^{-6}]}{\beta_3^*[Cl^-]^3 + \beta_4^*[Cl^-]^4 + \beta_5^*[Cl^-]^5 + \beta_6^*[Cl^{-6}]}\right\} = 0 \quad [A8]$$

For each solution composition (c_{SbCl_3}) the chloride concentration $[Cl^-]$ was determined from the zero intercept of Eq. A-8 with chloride concentration $[Cl^-]$. Subsequently, the concentrations of free bismuth ions $[Bi^{3+}]$ and free antimony ions $[Sb^{3+}]$ were calculated from Eq. 4 and 5. The concentration of each bismuth and antimony chloride complex, $BiCl_n^{3-n}$ and $SbCl_n^{3-n}$, was then calculated from the relevant stability constant β_n.

References

1. B. Lenoir, H, Scherrer, and T. Calliat, in *Semiconductors and Semimetals, Vol. 69: Recent Trends in Thermoelectric Materials Research I*, p. 101, Terry M. Tritt, Editor, Academic Press, New York (2001).
2. M. S. Dresselhaus, *J. Phys. Chem. Solids*, **32**, 3 (1971).
3. G. E. Smith, G. A. Baraff, and J. M. Rowell, *Phys. Rev.*, **135**, A1118 (1964).
4. P. B. Alers and R. T. Webber, *Phys. Rev.*, **91**, 1060 (1953).
5. J. H. Mangez, J.-P. Issi, and J. Heremens, *Phys. Rev. B*, **14**, 4381 (1976).
6. D. L. Partin, J. Heremans, D. T. Morelli, C. M. Thrush, C. H. Olk, and T. A. Perry, *Phys. Rev. B*, **38**, 3818 (1988).
7. F. Y. Yang, K. Liu, K. Hong, D. H. Reich, P. C. Searson, and C. L. Chien, *Phys. Rev. Lett.*, **82**, 3328 (1999).
8. F. Y. Yang, K. Liu, K. Hong, D. H. Reich, P. C. Searson, and C. L. Chien, *Science*, **284**, 1335 (1999).
9. P. M. Vereecken and P. C. Searson, *Appl. Phys. Lett.*, **75**, 3135 (1999).
10. P. M. Vereecken, L. Sun, P. C. Searson, M. Tanase, D. H. Reich, and C. L. Chien, *J. Appl. Phys.*, **88**, 6529 (2000).

11. C. L. Chien, F. Y. Yang, K. Liu, D. H. Reich, and P. C. Searson, *J. Appl. Phys.*, **87**, 4659 (2000).
12. R. Walker and S. J. Snook, *Met. Finish.*, **June**, 79 (1980).
13. K. B. Morris, D. Z. Douglass, and C. B. Vaughn, *J. Electrochem. Soc.*, **101**, 343 (1954).
14. S. I. C. de Torresi and I. A. Carlos, *J. Electroanal. Chem.*, **414**, 11 (1996).
15. T. Valkova and I. Krastev, *Trans. Inst. Met. Finish.*, **80**, 16 (2002).
16. R. K. Iyer and S. G. Deshpande, *J. Appl. Electrochem.*, **17**, 936 (1987).
17. Y. N. Sadana, J. P. Singh, and R. Kumar, *Surf. Technol.*, **24**, 319 (1985).
18. F. Besse, C. Boulanger, and J. M. Lecuire *J. Appl. Electrochem.*, **30**, 385 (2000).
19. *Standard Potentials in Aqueous Solutions*, p. 185, A. J. Bard, R. Parsons, and J. Jordan, Editors, Marcel Dekker, New York (1985).
20. F. Pantani and P. G. Desideri, *Gazzetta*, **89**, 1360 (1959).
21. *Atlas of Electrochemical Equilibria in Aqueous Solutions*, M. Pourbaix, Editor, Pergamon Press, Oxford, U.K. (1966).
22. *Encyclopedia of Electrochemistry of Elements*, Vol. IX B, A. J. Bard, Editor, Marcel Dekker, New York (1973).
23. *Encyclopedia of Electrochemistry of Elements*, Vol. IV, A. J. Bard, Editor Marcel Dekker, New York (1973).
24. *Tables of Standard Electrode Potentials*, G. Milazzo and S. Caroli, Wiley, New York (1978).
25. M. Noel and K. I. Vasu, *Cyclic Voltammetry and the Frontiers of Electrochemistry*, Chap. 7, Aspect Publications, London (1990).
26. J. C. Patrin, Y. Z. Li, M. Chander, and J. H. Weaver, *J. Vac. Sci. Technol. A*, **11**, 2073 (1993).
27. M. Naitoh, H. Shimaya, S. Nishigaki, N. Oishi, and F. Shoji, *Surf. Sci.*, **377**, 899 (1997).
28. D. Gonnissen, W. Simons, and A. Hubin, *J. Electroanal. Chem.*, **435**, 149 (1997).